RSC Advances

PAPER

View Article Online
View Journal | View Issue

Cite this: *RSC Adv.*, 2024, **14**, 17855

Enhanced electrochemical performance of Ce-MOF/h-CeO_2 composites for high-capacitance energy storage applications†

Ruhani Baweja, [a] Monika Verma, [bc] Sanjeev Gautam, *[b] Shailesh Upreti[d] and Navdeep Goyal [a]

The escalating demand for energy storage underscores the significance of supercapacitors as devices with extended lifespans, high energy densities, and rapid charge–discharge capabilities. Ceria (CeO_2), known for its exceptional properties and dual oxidation states, emerges as a potent material for supercapacitor electrodes. This study enhances its capacitance by integrating it with Metal–Organic Frameworks (MOFs), carbon-rich compounds noted for their good conductivity. In our research, hollow ceria (h-ceria) is synthesized *via* hydrothermal methods and amalgamated with Ce-MOF, employing 2,6-dinaphthalene dicarboxylic acid as a ligand, to fabricate Ce-MOF@h-CeO_2 composites. The structural and morphological characteristics of the composite are methodically examined using X-ray Diffraction (XRD), Field Emission Scanning Electron Microscopy (FE-SEM), and Fourier-Transform Infrared (FT-IR) spectroscopy. The band gap of the materials is ascertained through UV-Diffuse Reflectance Spectroscopy (UV-DRS). Electrochemical behavior and redox properties of the Ce-MOF composites are explored using Cyclic Voltammetry (CV), Galvanostatic Charge and Discharge (GCD), and Electrochemical Impedance Spectroscopy (EIS), providing insights into the material's stability. Electrochemical characterization of the composite reveals maximum specific capacitance, energy density and power density are 2643.78 F g^{-1} at a scan rate of 10 mV s^{-1}, 249.22 W h kg^{-1}, and 7.9 kW kg^{-1}, respectively. Additionally, the specific capacitance of Ce-MOF synthesized with a 2,6-dinaphthalene dicarboxylic acid (NDC) ligand reaches 995.59 F g^{-1}, surpassing that of Ce-MOF synthesized using a 1,3,5-tricarboxylic acid (H_3BTC) ligand. These findings highlight the promising economic potential of high-performance, environmentally sustainable, and cost-effective energy storage devices. The innovative Ce-MOF@h-CeO_2 composite materials at the core of this research pave the way for advancing the field of energy storage solutions.

Received 20th January 2024
Accepted 27th May 2024

DOI: 10.1039/d4ra00523f

rsc.li/rsc-advances

1 Introduction

The burgeoning energy demands of the modern era, driven by the increased use of electronic devices, are leading to the depletion of fossil fuels. Concurrently, the detrimental impact of non-renewable energy sources on both humanity and the environment necessitates a re-evaluation of energy sources, propelling a shift towards renewable resources. These alternatives include wind, hydrothermal, and solar energy (either harnessed through photovoltaic systems[1] or through concentrated solar power plants[2]), as well as thermoelectric energy[3] and others.[4,5] This escalating energy requirement has drawn attention towards energy storage devices, particularly supercapacitors and batteries.[6–8] Supercapacitors, being an advanced technology, are preferred for their exceptional characteristics such as power density, long cycle life, rapid charge–discharge rates, and high specific capacity.[9,10]

Although specific capacity depends upon many factors, electric double-layer capacitors (EDLCs) and pseudocapacitors generally have higher capacities compared to hybrid supercapacitors.[10,11] EDLCs store charge *via* the reversible adsorption of electrolyte ions at the electrode–electrolyte interface,[12,13] offering rapid charging and longer cycle stability, albeit with lower energy density. Pseudocapacitors, in contrast, utilize reversible faradaic reactions for charge storage,[14] providing higher energy density and specific capacity but at the expense of cycle life and conductivity. Hybrid supercapacitors combine the attributes of both EDLCs and pseudocapacitors.[15] Potential materials for EDLC electrodes include carbon-based substances like graphene and

[a]*Department of Physics, Panjab University, Chandigarh 160014, India*
[b]*Advanced Functional Materials Lab, Dr S. S. B. University Institute of Chemical Engineering & Technology, Panjab University, Chandigarh 160014, India. E-mail: sgautam@pu.ac.in; Tel: +91 97797 13212*
[c]*Energy Research Centre, Panjab University, Chandigarh 160014, India*
[d]*Charge CCCV (C4V), Center of Excellence, Binghamton University, 45 Murray Hill Road, Vestal, NY 13850, USA*

† Electronic supplementary information (ESI) available. See DOI: https://doi.org/10.1039/d4ra00523f

carbon nanotubes (CNT), while conductive polymers[16] and transition metal oxides/hydroxides[17] are suitable for pseudocapacitor electrodes. However, there is a continuous search for materials that can further enhance the efficiency of supercapacitors, including hybridizing high surface area materials from EDLCs with compounds used in pseudocapacitor electrodes.[18]

Considering suitable materials, metal–organic frameworks (MOFs) are emerging as a novel class of porous materials composed of metal ions or clusters coordinated to organic ligands, forming diverse structural dimensions.[19,20] Their distinctive properties such as high surface area, porosity, thermal stability, and modifiability make them suitable for various energy and environmental applications.[21] Nevertheless, their electrochemical application is limited due to low electrical conductivity.[22] Transforming MOFs into other materials like metal oxides, porous carbon, metal hydroxides,[23] phosphides,[24] sulfides,[25] selenides,[26] or composites,[27] has been a researched focus to overcome these constraints. For example, doping Ni-based MOFs with Zn ions[28] significantly increased their capacitance.

Cerium oxide (CeO_2), known as ceria, is noted for its affordability, non-toxicity, abundance, and ability to undergo reversible transitions between Ce^{3+} and Ce^{4+} states, alongside high oxygen storage capacity,[29] making it suitable for supercapacitor applications. Reported[30] specific capacitance of cerium oxide sheets is 481 F g^{-1} at a scan rate of 5 mV s^{-1}, retaining about 83% capacity after 500 cycles. Transition metal-doped MOFs have shown promise as supercapacitor electrodes, with specific capacitance values ranging significantly.[31] Yet, lanthanide-based MOFs, such as Ce-MOF, have been less explored, with Ce-MOF showing superior performance and retention.[20] Combining ceria with MOFs (CeO_2-MOFs) offers a novel approach to enhance supercapacitor efficiency.

This research details the development of a supercapacitor electrode, ceria-based Ce-MOF using the NDC ligand, and the successful creation of Ce-MOF@h-CeO_2 composites with a distinctive hollow structure. The hypothesis posits that Ce-MOF contributes to redox reactions and ion diffusion, while the CeO_2 component is responsible for boosting the electrical conductivity of the composite.

This investigation involves conducting diverse characterizations, including XRD and FE-SEM, to ascertain the properties of the material under examination. Furthermore, cyclic voltammetry studies are conducted to identify the specific capacity of the samples. The primary goal of this research is to identify materials with high capacity to fulfill energy requirements. The specific capacitance is expected to escalate with the addition of h-ceria into the Ce-MOF. Moreover, the comparison between the capacitance of Ce-MOF with 2,6-dinaphthalene dicarboxylic acid ligand and 1,3,5-tricarboxylic acid is made using CV analysis.

2 Experimental details

2.1 Materials

All reagents were obtained from Sigma-Aldrich with a 4 N purity and were used as received. The reagents included cerium nitrate hexahydrate ($Ce(NO3)_3 \cdot 6H_2O$), acetic acid (CH_3COOH), ethylene glycol ($C_2H_6O_2$), polyvinyl pyrrolidone (PVP, K-25), and 2,6-naphthalene dicarboxylic acid ($C_{12}H_8O_4$).

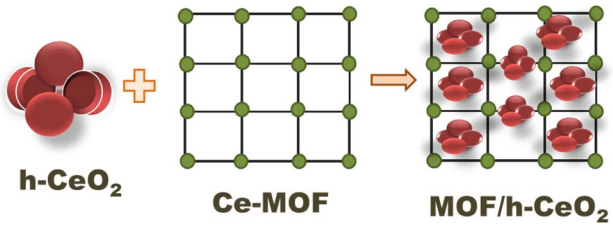

Fig. 1 Schematic diagram of the synthesis route of Ce-MOF@h-CeO_2 with the hollow structure using hydrothermal method.

2.2 Synthesis of hollow ceria

Hollow ceria (h-CeO_2) was synthesized following a modified version of the method reported by Jiang *et al.*[32] Initially, 2.0 g of $Ce(NO_3)_3 \cdot 6H_2O$ and 16 ml of deionized water were mixed in 40 ml of ethylene glycol in a beaker and stirred for approximately one hour to achieve a homogeneous solution. Subsequently, 2 ml of acetic acid was gradually added and stirred for 15 minutes. Next, 1.6 g of PVP (K-25) was added and stirred for 20 minutes. The mixture was then transferred to a 100 ml Teflon-lined stainless-steel autoclave. The autoclave was maintained at 180 °C for 22 hours before cooling to room temperature. The resulting products were centrifuged, repeatedly rinsed with deionized water about 6–7 times, dried at 80 °C for 14 hours, and finally calcined at 500 °C for 4 hours in air to yield CeO_2 microspheres.

2.3 Synthesis of Ce-MOF

Ce-MOF was synthesized using a hydrothermal method.[33] A mixture of 0.04 g $Ce(NO_3)_3 \cdot 6H_2O$ and 0.2 g of 2,6-naphthalene dicarboxylic acid in 40 ml of deionized water was sonicated for about 30 minutes to form solution 'X'. This solution was then transferred to a 100 ml Teflon-lined stainless-steel autoclave and heated at 60 °C for 20 hours. After naturally cooling to room temperature, the product was centrifuged, washed with deionized water approximately 6–7 times, and oven dried at 60 °C for 24 hours.

2.4 Synthesis of Ce-MOF/h-CeO_2

The schematic for the synthesis of Ce-MOF/h-CeO_2 composites is illustrated in Fig. 1.[33] Solution 'X' was prepared as described, and a predetermined quantity of h-CeO_2 ($Y = 0.05, 0.10$ g) was added and thoroughly mixed. The solution was then transferred to a 100 ml Teflon-lined stainless-steel autoclave and maintained at 60 °C for 20 hours. Upon cooling to room temperature, the product was centrifuged, washed with deionized water, and dried at 80 °C for 24 hours. The resultant samples were denoted as Ce-MOF/h-CeO_2-1 and Ce-MOF/h-CeO_2-2, respectively.

3 Characterization

3.1 Materials characterization

The structural and compositional characteristics of the fabricated samples were examined using X-ray diffraction (XRD) on

a PANalytical (Netherlands) X'pert Pro model. Measurements were taken over a Bragg angle range of 5° to 80° at a scanning rate of 1° min^{-1}, ensuring detailed structural resolution suitable for Rietveld refinement. The XRD data facilitated crystal phase identification and were further analyzed for Rietveld refinement using the FullProf Suite-2021.[34]

Field Emission Scanning Electron Microscopy (FE-SEM) images and Energy Dispersive Spectroscopy (EDS) analyses of the synthesized samples were conducted on a Hitachi (Japan) Model-SU 8010 series, offering a resolution of 1 nm at a landing voltage of 1 kV for morphological studies. UV-DRS spectroscopy was employed to determine the band gaps of the samples, using $BaSO_4$ as a reference. This was performed on a UV-2600 Shimadzu spectrophotometer across the wavelength range of 200–700 nm. For functional group identification, a PerkinElmer Spectrum-400 FT-IR spectrometer was used alongside KBr powder as the standard reference. The samples were thoroughly mixed with KBr, finely ground to produce a uniform powder, and subsequently compressed into pellets.

3.2 Electrochemical measurements

Electrochemical characterization of the prepared samples was performed using cyclic voltammetry, galvanostatic charge–discharge, and electrochemical impedance spectroscopy techniques to determine the conductivity of the nanocomposites. These measurements were conducted using a Potentiostat/Galvanostat M204 (Metrohm Autolab, central facility lab (TEQIP-III), Dr SSB UICET, Panjab University, Chandigarh).[35] The experimental setup utilized a three-electrode system, comprising a platinum coil counter-electrode, an Ag/AgCl reference electrode, and a working electrode.

The working electrode was prepared by depositing an ink, made from the sample, onto a glassy carbon electrode using the drop casting method. The ink was prepared by dissolving 3 mg of the active material in ethanol to form a homogeneous mixture after sonicating for 30 minutes. Using a micropipette, the ink was drop-cast onto the working electrode and allowed to dry to form a uniform layer. This process was repeated 3–4 times until a uniform layer was formed. The electrochemical analysis using CV was conducted over a potential range of −0.1 V to 1.0 V at various scan rates, *i.e.* 10, 20, 30, 40, 50, and 100 mV s^{-1}, and GCD technique at various current densities of 1, 2, 3, 3.5, and 4 A g^{-1}. The samples were used without a binder as the material is quite stable, adheres easily to the working electrode and maintain a good stability (contstant electric contact) at the interface between working electrode and deposit materials.

4 Results and discussion

4.1 X-ray diffraction measurements and Rietveld analysis

X-ray diffraction (XRD) was employed to examine the structure of the materials, evaluating aspects such as crystallinity, nanoparticle size, phase purity, and lattice parameters.

The XRD patterns of h-CeO_2 were consistent with the cubic phase of the cerium oxide structure (JCPDS No. 03-065-5923).[36] The peaks at 28.6°, 33.1°, 47.5°, 58.9°, and 69.4° correspond to the (111), (200), (220), (311), and (222) planes, respectively, as depicted in Fig. 2(a). The dominant peak at $2\theta = 28.6°$ corresponds to the (111) plane. Ce-MOF exhibited characteristic diffraction peaks at 11.83°, 15.24°, 26.73°, and 30.81°, which were slightly shifted (revealing substitutional doping of larger ceria atomic radii) from those reported in the literature.[33] The Ce-MOF/h-CeO_2 composites displayed distinct peaks for both h-CeO_2 and Ce-MOF structures, with no impurity peaks, indicating single-phase (purity) and good crystallinity.

Crystallite size was determined using Scherrer's equation: $D = k\lambda/\beta \cos \theta$, where D is the crystallite size (nm); k is the shape factor (0.9); λ is the X-ray wavelength (0.154056 nm for Cu K_α radiation); θ is the Bragg angle; and β is the full width at half maximum (FWHM in radians).[37] The average crystallite size of h-ceria is determined to be 18.88 nm.

Rietveld refinement was used for quantitative phase analysis,[38,39] adjusting XRD data using standard lattice parameters. The experimental XRD patterns were precisely fitted by refining the structural parameters of simulated patterns (Fig. 2(b)). FullProf 2021 software was used for refinement, and step-scan data were recorded from 20° to 80° (step size 0.017°). The refinement was executed considering the cubic crystal structure (space group $Fm\bar{3}m$) of CeO_2 [40] with standard lattice parameters $a = b = c = 5.4037$ Å. The calculated lattice parameters were $a = b = c = 5.4128$ Å, and the unit cell volume was 158.589 $Å^3$. The crystal structure (Fig. 2(c) and (d)) was generated from the cif file obtained from the simulated pattern, revealing the exact position coordinates of one cerium atom and two oxygen atoms present in the ceria system. This cif file is deposited at CCDC, UK (2359413) and also included in the ESI.† The XRD pattern confirms the phase corresponding to the space group "$Fm\bar{3}m$", indicative of pure CeO_2 nanoparticles.

Table 1 details the unit cell constraints derived from Rietveld refinement, including positional and atomic parameters. The R-factors obtained from the refinement (R_p, R_{wp}, R_{exp}) were 27.5, 20.8, and 19.7, respectively. Other fitting parameters such as χ^2 was 1.11 and G.O.F was 1.1, as shown in Fig. 2(b).

4.2 Morphology and composition analysis

Field Emission Scanning Electron Microscopy (FE-SEM) images of h-CeO_2, Ce-MOF, and Ce-MOF/h-CeO_2 composites (Ce-MOF/h-CeO_2-1 and Ce-MOF/h-CeO_2-2) are presented in Fig. 3. The FE-SEM image of h-CeO_2 displays uniformly dispersed microspheres with an average diameter of approximately 19–20 nm. Ce-MOF exhibits a diamond-like morphology with an average diameter of about 3 μm. The SEM images of Ce-MOF/h-CeO_2-1 and -2 show a similar morphology to Ce-MOF, with ceria microspheres attached to the surface, resulting in an increased particle size. The consistent morphology across the Ce-MOF/h-CeO_2 composite suggests successful synthesis, with the Ce-MOF homogeneously distributed over the h-CeO_2 surface.[33]

Particle size was analyzed using ImageJ Ver 1.53t software. It was observed that as the concentration of h-CeO_2 in the Ce-MOF composites increased, the average particle size decreased, approaching that of pure ceria.

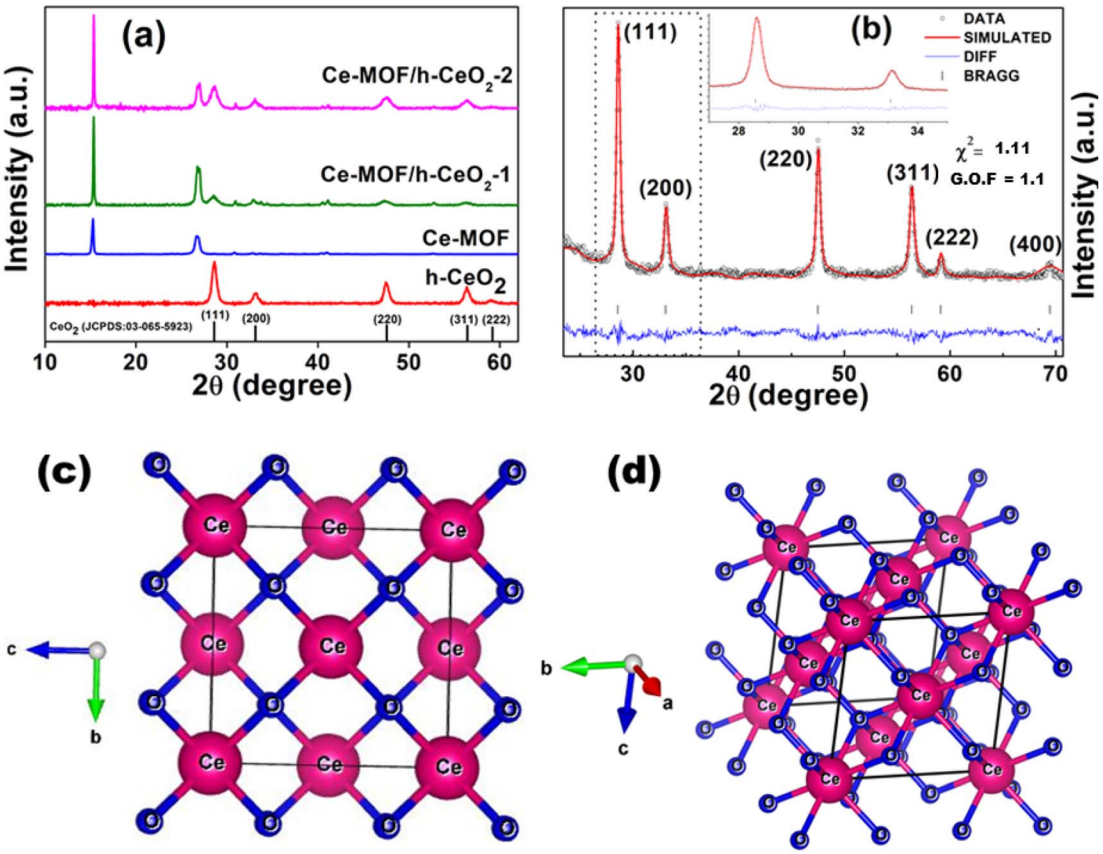

Fig. 2 (a) X-ray diffraction patterns of h-ceria, Ce-MOF, Ce-MOF/h-CeO_2-1, and Ce-MOF/h-CeO_2-2; (b) simulated XRD pattern output from Rietveld analysis of h-CeO_2, where χ^2 and G.O.F. values indicate the quality of XRD data for synthesized samples; (c) and (d) crystal structure representation obtained through Rietveld analysis.

Table 1 Rietveld refined atomic parameters of CeO_2 crystal structure were χ^2 – 1.11 and G.O.F – 1.1, the various *R*-factors obtained for h-ceria, *i.e.* R_p, R_{wp}, R_{exp} are 27.5, 20.8, 19.7, respectively

Atom	*x*	*y*	*z*	Occupancy
Ce	0.00000	0.00000	0.00000	1.000
O	0.25000	0.25000	0.25000	1.032

The particle size distribution of h-CeO_2, Ce-MOF, Ce-MOF/h-CeO_2-1, and Ce-MOF/h-CeO_2-2, as derived from FE-SEM image analysis with ImageJ 1.53t, is depicted in Fig. 3(e)–(h). The histogram-based calculations from the FE-SEM image of h-ceria align closely with the results obtained from Rietveld analysis. Both methods demonstrate a consistent trend in particle size variation among the different samples.

Energy Dispersive Spectroscopy (EDS) was conducted to analyze the elemental composition of all synthesized samples: h-CeO_2, Ce-MOF, Ce-MOF/h-CeO_2-1, and Ce-MOF/h-CeO_2-2. The EDS spectrum of the h-CeO_2 sample, as shown in Fig. S1(a) (in ESI text†), confirmed the presence of only Ce and O, with no detectable impurity elements. Similarly, the EDS spectra for Ce-MOF and its composites, presented in Fig. S1(b)–(d) (in ESI text†), revealed the presence of Ce, O, and C in varying molar ratios, without any evidence of extraneous or impure peaks.

4.3 UV-diffuse reflectance spectroscopy (UV-DRS)

The optical properties of h-CeO_2, Ce-MOF, and Ce-MOF/h-CeO_2 composites (Ce-MOF/h-CeO_2-1 and Ce-MOF/h-CeO_2-2) were investigated using UV-Diffuse Reflectance Spectroscopy (UV-DRS) in the wavelength range of 300–700 nm. As depicted in Fig. 4(a), the primary optical absorption of these samples is situated in the ultraviolet region. The absorption edge wavelengths for h-CeO_2, Ce-MOF, Ce-MOF/h-CeO_2-1, and Ce-MOF/h-CeO_2-2 composites are 443.01 nm, 424.65 nm, 427.58 nm, and 435.08 nm, respectively.

The optical band gap energy (*Eg*) of these samples was calculated using the equation: $(\alpha h\nu)^{1/2} = A(h\nu - E_g)$, where $h\nu = 1240/\lambda$. In this equation, α represents the absorption coefficient, h is Planck's constant, λ signifies the absorption edges, and A is a constant.[36] The calculated band gap energies for h-CeO_2, Ce-MOF, Ce-MOF/h-CeO_2-1, and Ce-MOF/h-CeO_2-2 composites were found to be 2.71 eV, 2.86 eV, 2.78 eV, and 2.75 eV, respectively, as illustrated in Fig. 4(b).

4.4 FT-IR spectra

Fourier-Transform Infrared (FT-IR) spectroscopy was employed to investigate the chemical functional groups present in the synthesized samples, namely h-CeO_2, Ce-MOF, and Ce-MOF/h-CeO_2 composites (Ce-MOF/h-CeO_2-1 and Ce-MOF/h-CeO_2-2), as

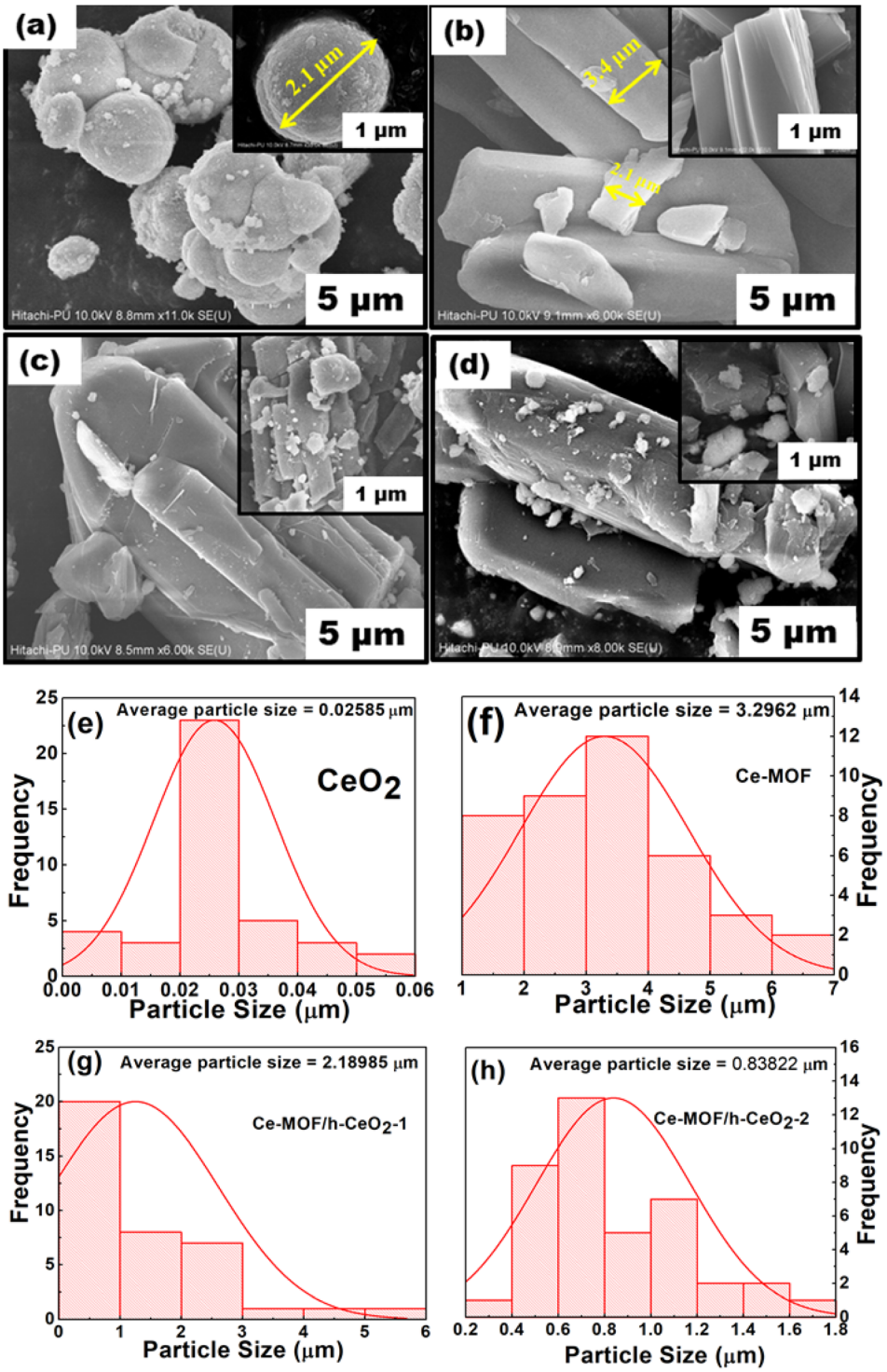

Fig. 3 FE-SEM micrographs of (a) h-ceria, (b) Ce-MOF, (c) Ce-MOF/h-CeO_2-1 and (d) Ce-MOF/h-CeO_2-2; particle size distribution histogram of (e) h-ceria, (f) Ce-MOF, (g) Ce-MOF/h-CeO_2-1, and (h) Ce-MOF/h-CeO_2-2.

illustrated in Fig. 4(c). Peaks observed in the range of 1612–1557 cm^{-1} and 1435–1373 cm^{-1} are attributed to the asymmetric and symmetric stretching of carboxylate ions,[41] respectively. The O–H stretching vibrations[42] are identified in the range of 3300–3500 cm^{-1}, and the C=O stretching vibration[41] is noted at 1686.1 cm^{-1}. Additionally, the region between 500–850 cm^{-1} is indicative of Ce–O stretching vibrations,[43] confirming the presence of ceria in the composites.

4.5 Electrochemical characterization

4.5.1 Cyclic voltammetry (CV) analysis. Cyclic voltammetry (CV) was employed to assess the conductivity of the prepared

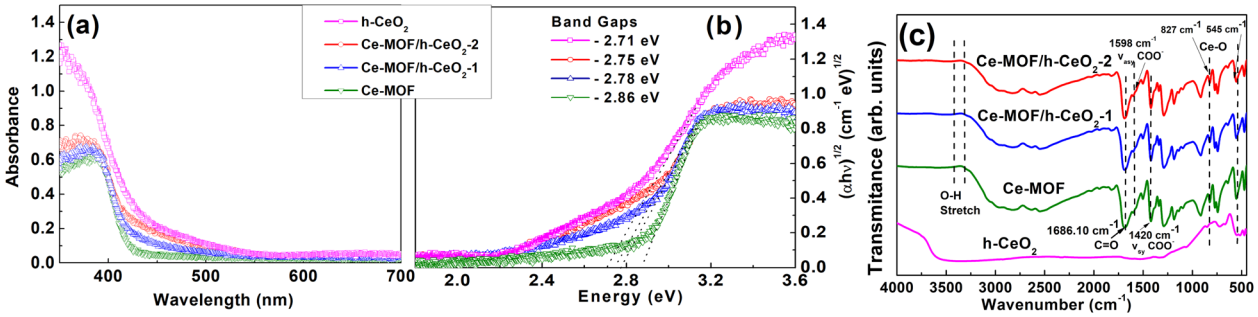

Fig. 4 (a) UV-DRS spectra, (b) band gap, and (c) FT-IR spectra of h-ceria, Ce-MOF, Ce-MOF/h-CeO_2-1, and Ce-MOF/h-CeO_2-2.

nanocomposites. While the primary intent of CV is to probe the electrochemical behavior of the samples, such analysis inherently provides insights into the materials' conductivity. The redox processes and charge transfer kinetics during cyclic voltammetry, the efficiency of charge carriers' movement within the nanocomposites can be assessed. Therefore, CV serves as a tool to delve into the electrochemical characteristics of the nanocomposites, offering valuable information about conductivity, as higher peak currents indicate higher conductivity, which is crucial for their potential applications. Additionally, CV provides insights into the cyclic stability of the prepared samples and explains the behavior of the electrode material. In this case, the material behaves as a pseudocapacitive material.

Cyclic voltammetry (CV) curves were analyzed for the prepared samples, which are h-CeO_2, Ce-MOF, Ce-MOF/h-CeO_2-1, and Ce-MOF/h-CeO_2-2. The CV measurements were conducted at different scan rates of 10, 20, 30, 40, 50, and 100 mV s^{-1} within the potential range of −0.1 to 1.0 V, as shown in Fig. 5(e).

The specific capacitance (C_s) of the materials[42] can be calculated using eqn (3), derived from the fundamental eqn (1):

$$I = C_s m k \quad (1)$$

integrating both sides with respect to the voltage (V) gives:

$$A = (V_2 - V_1) C_s m k \quad (2)$$

here, $A = \int i\,dV$ represents the integrated area under the CV curve, and the total contribution from both the charging ($A_1 = (V_2 - V_1)Csmk$) and discharging ($A_2 = (V_1 - V_2)C_s mk$) phases is considered to obtain:

$$C_s = \frac{\int i\,dV}{2mk\Delta V} \quad (3)$$

in this equation, $\int i\,dV$ is the integrated area under the CV curve, m (g) is the mass of the active material, ΔV (V) denotes the width of the potential window, and k (V s^{-1}) is the scan rate.

The CV curves obtained at different scan rates (10, 20, 30, 40, 50, and 100 mV s^{-1}) for h-CeO_2, Ce-MOF, Ce-MOF/h-CeO_2-1, and Ce-MOF/h-CeO_2-2 are shown in Fig. 5(a)–(d). The specific capacitance (C_s) values for h-CeO_2, Ce-MOF, Ce-MOF/h-CeO_2-1, and Ce-MOF/h-CeO_2-2 were measured as 1581.52 F g^{-1}, 995.59 F g^{-1},[42] 2575.74 F g^{-1}, and 2643.78 F g^{-1}, respectively, at a scan rate of 10 mV s^{-1}. Specific capacitance values at the mentioned scan rates were calculated using eqn (3), and are presented in Table 2. The table reveals that the specific capacitance of samples decreases with increasing scan rates. This decrease is attributed to two factors: at lower scan rates, lower resistance and the kinetic energy of ions allow for extended interaction time with the electrode surface; conversely, at higher scan rates, ions have less time to interact with the electrode due to increased kinetic energy and resistance, thereby reducing specific capacitance.

Furthermore, the maximum specific capacitance of Ce-MOF, synthesized with 2,6-dinaphthalene dicarboxylic acid as the ligand, is found to be 995.59 F g^{-1} at a scan rate of 10 mV s^{-1}. This is higher compared to that obtained for Ce-MOF with 1,3,5-tricarboxylic acid.[42,44] This difference in capacitance is attributed to the higher number of active sites in 2,6-dinaphthalene dicarboxylic acid compared to 1,3,5-tricarboxylic acid, as illustrated in Fig. S2 (in the ESI text†).

It was determined from the CV that the electrode (working) gives almost the same results even after 50 cycles, which shows its cyclic stability as it decomposes less with time, as shown in Fig. S3(a) (in the ESI text†). The deviation of the voltammogram shapes from an ideal rectangular form indicates that the capacitance is mainly derived from pseudocapacitance due to faradaic redox reactions of the electroactive materials.[45] Pseudocapacitors typically operate through three primary mechanisms for storing charge: monolayer adsorption, surface-level redox reactions, and intercalation/de-intercalation of ions within/from the electrode surface.[46] In this study, the relationship between peak current (I_P) and scan rate (ν) is modeled using the equation $I_P = a\nu^b$, where 'a' and 'b' are fitting parameters. The value of 'b' typically falls within the range of approximately 0.5 to 1 across all samples, indicating that both faradaic and non-faradaic charge storage mechanisms are at play. Since both mechanisms are active, all samples can be classified as pseudocapacitive in nature.

The respective equations for faradaic and non-faradaic charge storage processes are presented below, where 's' denotes the surface:[47]

Faradaic:

$$CeO_2 + H_2O + e^- \rightleftharpoons Ce^{3+}OOH \quad (4)$$

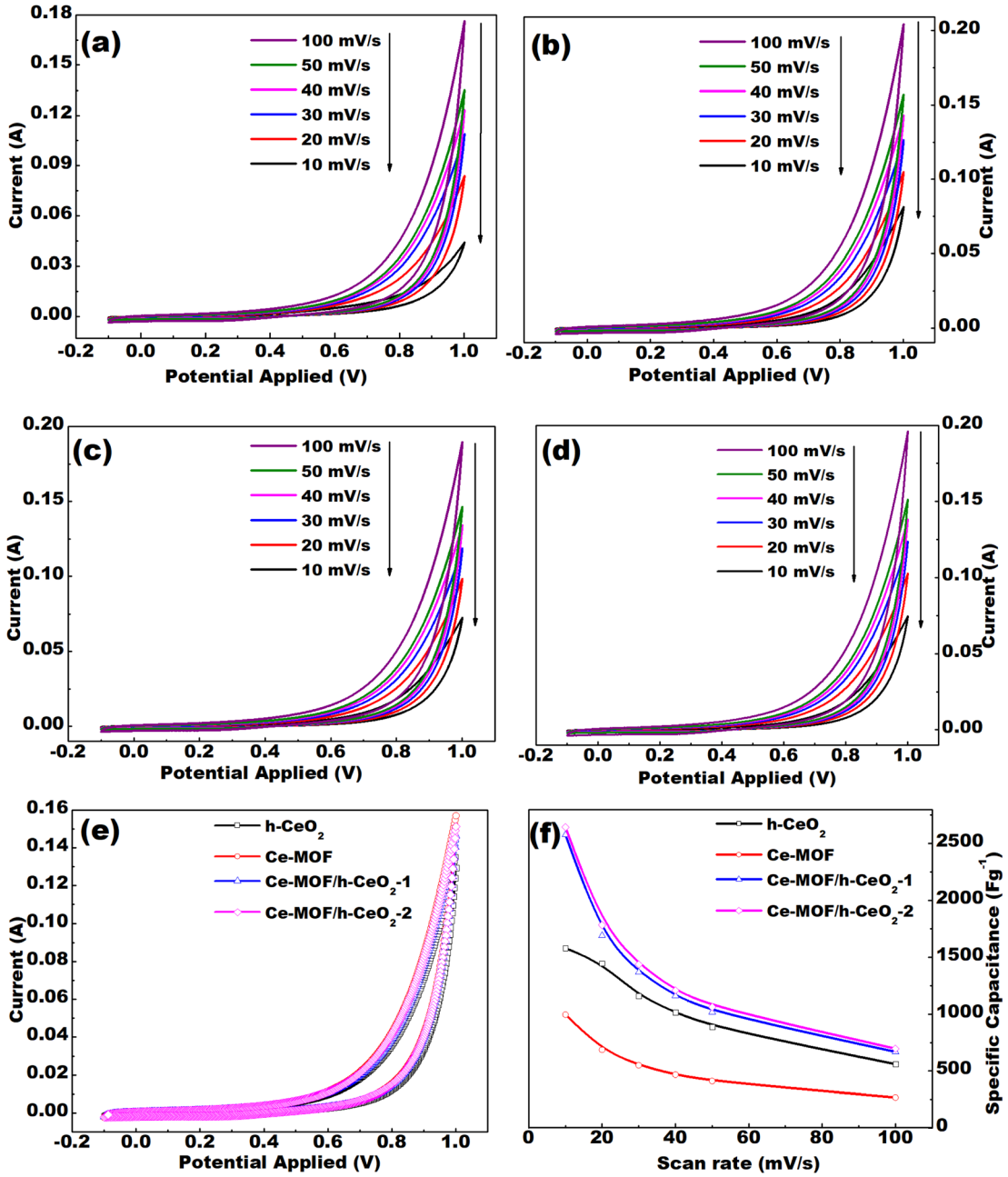

Fig. 5 CV curves of (a) h-CeO_2, (b) Ce-MOF, (c) Ce-MOF/h-CeO_2-1, (d) Ce-MOF/h-CeO_2-2 electrode at different scan rates; (e) comparison of CV curves for ceria, Ce-MOF, Ce-MOF/h-CeO_2-1 and Ce-MOF/h-CeO_2-2 at a scan rate of 50 mV s^{-1}; (f) comparison of specific capacitance at different scan rates for h-ceria, Ce-MOF, Ce-MOF/h-CeO_2-1 and Ce-MOF/h-CeO_2-2.

Table 2 Specific capacitance of h-ceria, Ce-MOF, Ce-MOF/h-CeO_2-1 and Ce-MOF/h-CeO_2-2 at different scan rates

	Specific capacitance (F g^{-1}) at different scan rate					
Sample	10 mV s^{-1}	20 mV s^{-1}	30 mV s^{-1}	40 mV s^{-1}	50 mV s^{-1}	100 mV s^{-1}
h-CeO_2	1581.52	1446.18	1160.29	1015.84	887.39	559.03
Ce-MOF	995.59	685.37	549.64	466.79	410.27	267.85
Ce-MOF/h-CeO_2-1	2575.74	1690.82	1368.32	1161.54	1018.16	667.67
Ce-MOF/h-CeO_2-2	2643.78	1782.71	1437.83	1210.15	1062.31	696.24

Non-faradaic:

$$(CeO_2)_s + K^+ + e^- \rightleftharpoons (CeO_2 \cdot K^+)_s \quad (5)$$

The peak current is plotted against the square root of the scan rate ($\nu^{1/2}$) to determine the diffusivity of the reactants, following the Randles–Sevcik equation,[48] as shown in Fig. S3(b) (in the ESI text†). Higher diffusivity indicates improved electrochemical performance of the material. Since Ce-MOF has better diffusivity compared to h-CeO_2, the addition of Ce-MOF to h-CeO_2 improves its diffusivity in the electrolyte and hence enhances its electrochemical performance.

4.5.2 Galvanostatic charge and discharge (GCD). Galvanostatic charge–discharge (GCD) is a fundamental technique used in electrochemical studies to characterize the performance of electrodes in energy storage devices, such as batteries and supercapacitors. In this method, the device is subjected to a constant current, known as the galvanostatic current, during both the charging and discharging processes. During charging, the device absorbs electrical energy, converting it into chemical energy, which is stored within the device's active materials. Conversely, during discharging, the stored energy is released as electrical current flows out of the device. Fig. 6(a)–(d) shows GCD curves of h-CeO_2, Ce-MOF, Ce-MOF/h-CeO_2-1, and Ce-MOF/h-CeO_2-2 at different current densities of 1, 2, 3, 3.5, and

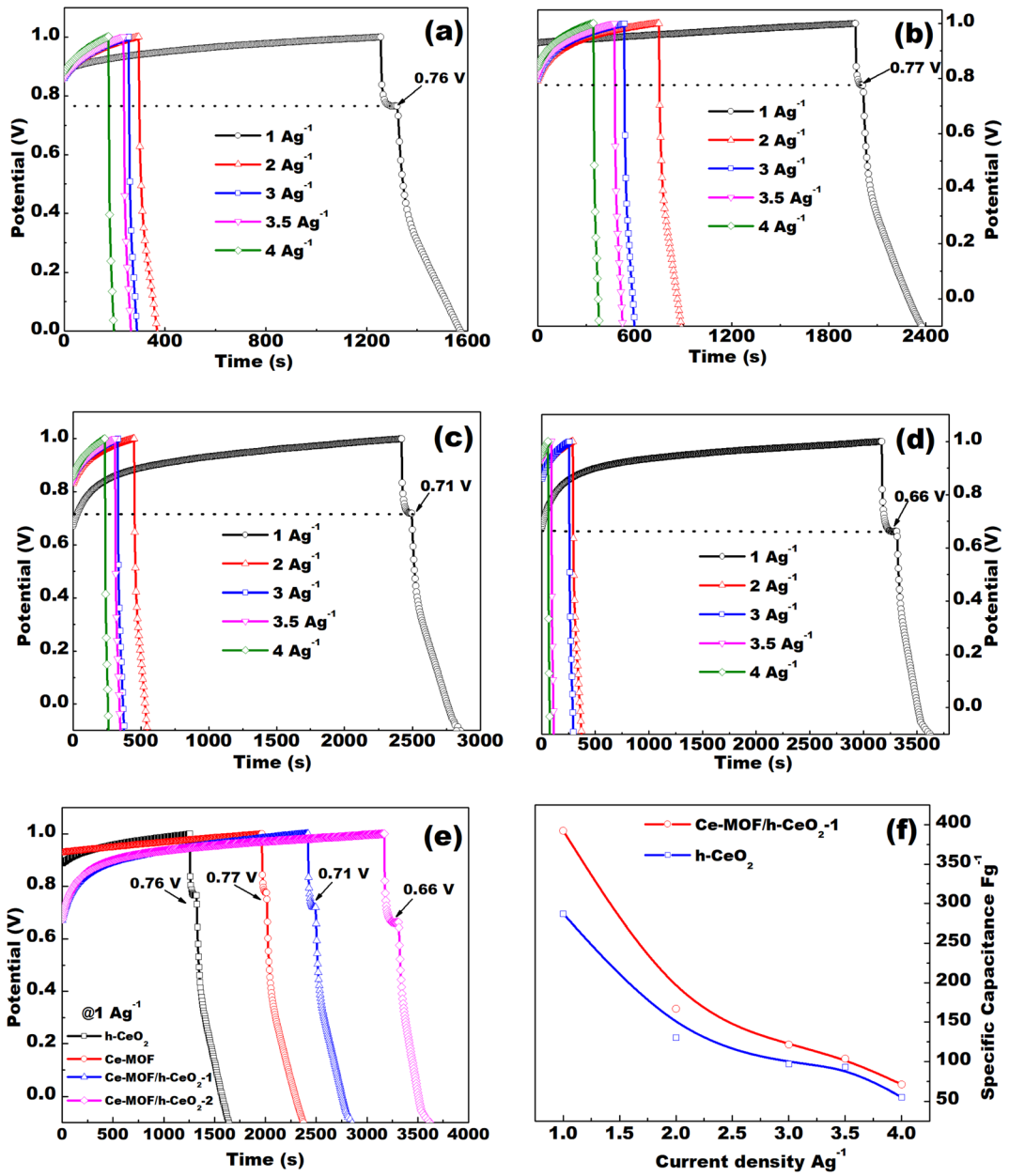

Fig. 6 GCD curves of (a) h-CeO_2, (b) Ce-MOF, (c) Ce-MOF/h-CeO_2-1, (d) Ce-MOF/h-CeO_2-2 electrode at different current densities in 3 M KOH; (e) comparison of GCD curves for h-ceria, Ce-MOF, Ce-MOF/h-CeO_2-1 and Ce-MOF/h-CeO_2-2 at a current density of 1 A g^{-1}; (f) comparison of specific capacitance at different current densities for h-ceria, and Ce-MOF/h-CeO_2-1.

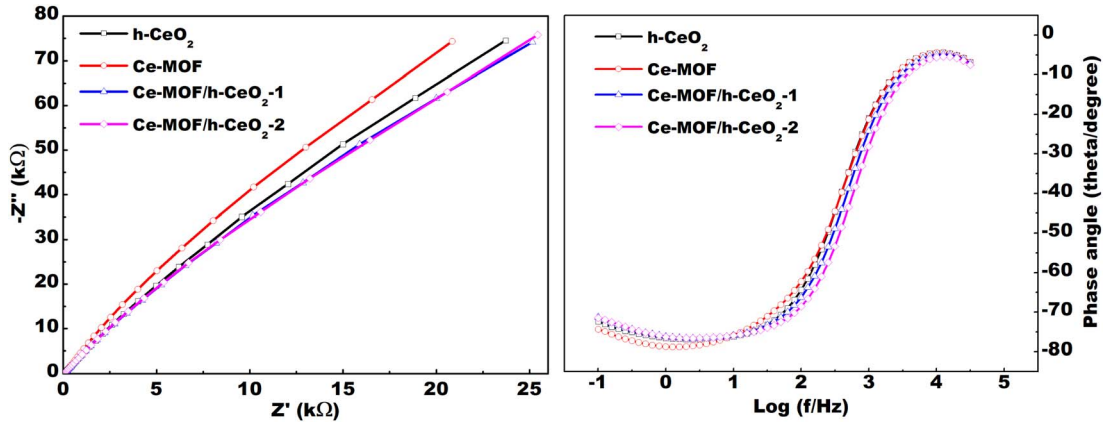

Fig. 7 (a) Nyquist plot, and (b) Bode phase angle of h-CeO_2, Ce-MOF, and their composites in 3 M KOH electrolyte.

4 A g^{-1} in 3 M KOH, respectively. The charge–discharge curves for all electrodes display a non-triangular shape, with distinct plateaus during discharge. This characteristic feature suggests the presence of pseudocapacitance behavior, attributed to the faradaic redox reaction of Ce^{2+}/Ce^{3+} with OH^-. This observation aligns well with the findings from cyclic voltammetry (CV) measurements. The plateau for different materials has different values and decreases with increasing concentration of h-CeO_2 in Ce-MOF. Fig. 6(e) shows the comparison of GCD curves of these materials at a current density of 1 A g^{-1}. From these plots, specific capacitance is calculated using eqn (6) and is found to be 287.24, 376.02, 392.26, and 411.94 F g^{-1}, for h-CeO_2, Ce-MOF, Ce-MOF/h-CeO_2-1, and Ce-MOF/h-CeO_2-2, respectively.

$$C_s = \frac{i\Delta t}{m\Delta V} \quad (6)$$

in this equation, Δt is the discharging time, m (g) is the mass of the active material, ΔV (V) denotes the width of the potential window, and i is the current density.

The specific capacitance decreases with an increase in current density, as shown in Fig. 6(f). The specific capacitance of Ce-MOF increases with the amount of h-CeO_2 added to it. The decrease in specific capacitance at high current densities likely arises from the challenge of electrolyte ions reaching the inner active sites of the electrode. In other words, the electrodes may not adequately facilitate full redox reactions at higher current densities due to the slower diffusion rate of OH^- ions into them.[49] Moreover, with an increase in current density, the specific capacitance of the electrodes diminishes as the interaction between the electrode and electrolyte ions decreases at higher current densities. Essentially, at lower current densities, electrolyte ions can readily diffuse into all available spaces on the electrode surface, facilitating ample insertion reactions.[50]

The energy and power density of Ce-MOF and its composites can be calculated using the following equations:

$$E = \frac{CV^2}{2} \quad (7)$$

in this equation, C is the specific capacitance, V is width of the potential window.

$$P = \frac{E}{t} \quad (8)$$

in this equation, E is the energy density, t is the discharging time.

Maximum energy density and power density of 249.22 W h kg^{-1} and 7.9 kW kg^{-1} were obtained for Ce-MOF/h-CeO_2 composite respectively, signifies it to be a high performance supercapacitor electrode.

4.5.3 Electrochemical impedance spectroscopy (EIS). Electrochemical impedance spectroscopy (EIS) was performed to investigate how the transport of charges in electrodes varied with frequency. By analyzing impedance variations across different frequencies, the research aimed to gain insights into the complex dynamics of electron movement within the electrode material. Fig. 7(a) shows the Nyquist plot of Ce-MOF composite electrodes measured with an AC perturbation of 0.01 V in the frequency range from 0.1 Hz to 10^5 Hz. The absence of a semicircular region in the high-frequency range indicates the presence of low faradaic charge transfer resistance,[51] while a vertical line in the low-frequency range indicates the ideal capacitive behavior of the electrodes.[52] Bode plot phase angles as a function of the frequency of the electrodes in 3 M KOH for the Ce-MOF composite electrodes are shown in Fig. 7(b). At low frequencies (<100 Hz), the phase angles of all electrodes fall within the 60°–80° range, indicating both redox and ideal capacitive behavior of the electrodes.[53] As the frequency rises (100–10^5 Hz), the phase angle decreases sharply, approaching zero in the frequency range of 10^4–10^5 Hz. This phenomenon can be attributed to reduced adsorption of electrolyte ions on the electrode surface, resulting in fewer accessible sites on the electrode. Consequently, the resistive component becomes dominant over the capacitive behavior, leading to a phase angle near zero in the high-frequency region.

5 Conclusions and future outlook

This study successfully synthesized Ce-MOF and h-ceria composites, incorporating up to 0.10 g of h-CeO_2, using a hydrothermal method. Lattice imperfections and structural

defects were analyzed through Rietveld refinement of XRD patterns, revealing the emergence of new peaks in Ce-MOF with increasing h-CeO_2 concentration. Morphological characteristics were ascertained using FE-SEM analysis, while UV-DRS spectroscopy and FT-IR analysis were employed to determine the band gap energies and functional groups of the composites, respectively. Notably, the data indicated a decrease in band gap energy with an increase in h-CeO_2 content.

The electrochemical performance of the samples was evaluated using cyclic voltammetry (CV), which demonstrated an increase in specific capacitance upon the introduction of h-CeO_2 into Ce-MOF. A significant specific capacitance of 2643.78 F g^{-1} was achieved at a scan rate of 10 mV s^{-1}. The maximum energy and power density were found to be 249.22 W h kg^{-1} and 7.9 kW kg^{-1}, respectively, using GCD analysis. The straight line Nyquist plots at high frequency region depicts low faradaic charge transfer resistance and may be useful in smart (memory) capacitor applications. All these electrochemical measurements indicate good pseudocapacitive behavior of Ce-MOF/h-CeO_2 electrodes and their potential for use in energy storage devices.

Future research endeavors could focus on further developing Ce-MOF/h-CeO_2 composites to enhance specific capacitance and overall efficiency of supercapacitors. Additionally, exploring other composites, such as those incorporating graphene oxide (GO) and carbon nanotubes (CNT), and comparing their performance could pave the way for more efficient energy storage devices. Since the maximum specific capacitance of Ce-MOF/h-CeO_2 composites is found to be 2643.78 F g^{-1}, it is expected to achieve supercapacitors with greater storage capacity with the addition of CNTs. These supercapacitors can further be used in conjunction with batteries in electric vehicles to provide bursts of power for acceleration and regenerative braking, enhancing the overall performance and efficiency of the vehicle.

Author contributions

Ruhani Baweja: writing – original draft, methodology, investigation, formal analysis, data mining. Monika Verma: methodology, investigation, data mining, discussions and writing-review & editing. Sanjeev Gautam: conceptualization, investigation, formal analysis, writing-review & editing, resources, funding acquisition, project administration and supervision. Navdeep Goyal: discussions, supervision, investigation and revisions. Shailesh Upreti: discussions, investigation and revisions.

Conflicts of interest

There are no conflicts to declare.

Notes and references

1 M. Verma and S. Gautam, *J. Magn. Magn. Mater.*, 2023, **588**, 171436.
2 S. Gautam, M. Verma, R. Chauhan, S. Aghara and N. Goyal, *Energy Adv.*, 2023, **2**, 1309–1325.
3 V. Thakur, K. Upadhyay, R. Kaur, N. Goyal and S. Gautam, *Mater. Today Adv.*, 2020, **8**, 100082.
4 Y. Zhao, F. Liu, K. Zhu, S. Maganti, Z. Zhao and P. Bai, *Adv. Compos. Hybrid Mater.*, 2022, **5**, 1537–1547.
5 Z. Sun, K. Qu, J. Li, S. Yang, B. Yuan, Z. Huang and Z. Guo, *Adv. Compos. Hybrid Mater.*, 2021, **4**, 1413–1424.
6 C. Hou, B. Wang, V. Murugadoss, S. Vupputuri, Y. Chao, Z. Guo, C. Wang and W. Du, *Eng. Sci.*, 2020, **11**, 19–30.
7 S. S. Patil, T. S. Bhat, A. M. Teli, S. A. Beknalkar, S. B. Dhavale, M. M. Faras, M. M. Karanjkar and P. S. Patil, *Eng. Sci.*, 2020, **12**, 38–51.
8 S. Singh, A. C. Rastogi, F. Omenya, M. S. Whittingham, A. Lal and S. Upreti, *MRS Online Proc. Libr.*, 2015, **1740**, mrsf14–1740.
9 S. Dai, Y. Bai, W. Shen, S. Zhang, H. Hu, J. Fu, X. Wang, C. Hu and M. Liu, *J. Power Sources*, 2021, **482**, 228915.
10 S. Gautam, S. Rialach, S. Paul and N. Goyal, *RSC Adv.*, 2024, **14**, 14311–14339.
11 Y. Ma, X. Xie, W. Yang, Z. Yu, X. Sun, Y. Zhang, X. Yang, H. Kimura, C. Hou, Z. Guo, et al., *Adv. Compos. Hybrid Mater.*, 2021, 1–19.
12 W.-C. Fang, *J. Phys. Chem. C*, 2008, **112**, 11552–11555.
13 K. Isakov, O. Sorsa, T. Rauhala, S. Saxelin, T. Kallio, H. Lipsanen and C. Kauppinen, *Energy Adv.*, 2022, **1**, 1041–1050.
14 Y. Wang, Y. Song and Y. Xia, *Chem. Soc. Rev.*, 2016, **45**, 5925–5950.
15 T. Liu, L. Zhang, W. You and J. Yu, *Small*, 2018, **14**, 1702407.
16 H. Gao and K. Lian, *RSC Adv.*, 2014, **4**, 33091–33113.
17 Y. Wang, Y. Lei, J. Li, L. Gu, H. Yuan and D. Xiao, *ACS Appl. Mater. Interfaces*, 2014, **6**, 6739–6747.
18 C. K. Maity, N. Goswami, K. Verma, S. Sahoo and G. C. Nayak, *J. Energy Storage*, 2020, **32**, 101993.
19 Z.-J. Lin, J. Lü, M. Hong and R. Cao, *Chem. Soc. Rev.*, 2014, **43**, 5867–5895.
20 S. Ghosh, A. De Adhikari, J. Nath, G. C. Nayak and H. P. Nayek, *ChemistrySelect*, 2019, **4**, 10624–10631.
21 Y. Wen, P. Zhang, V. K. Sharma, X. Ma and H.-C. Zhou, *Cell Rep. Phys. Sci.*, 2021, **2**, 100348.
22 G. Xu, C. Zhu and G. Gao, *Small*, 2022, **18**, 2203140.
23 H. B. Wu and X. W. Lou, *Sci. Adv.*, 2017, **3**, eaap9252.
24 W. Li, D. Xiong, X. Gao and L. Liu, *Chem. Commun.*, 2019, **55**, 8744–8763.
25 K. Wan, J. Luo, C. Zhou, T. Zhang, J. Arbiol, X. Lu, B.-W. Mao, X. Zhang and J. Fransaer, *Adv. Funct. Mater.*, 2019, **29**, 1900315.
26 K. Wan, J. Luo, X. Zhang, P. Subramanian and J. Fransaer, *J. Energy Chem.*, 2021, **62**, 198–203.
27 P. Li, R. Chen, S. Tian and Y. Xiong, *ACS Sustain. Chem. Eng.*, 2019, **7**, 9566–9573.
28 J. Yang, C. Zheng, P. Xiong, Y. Li and M. Wei, *J. Mater. Chem. A*, 2014, **2**, 19005–19010.
29 X.-Z. Song, W.-Y. Zhu, X.-F. Wang and Z. Tan, *ChemElectroChem*, 2021, **8**, 996–1020.
30 B. Talluri, K. Yoo and J. Kim, *Ceram. Int.*, 2022, **48**, 164–172.
31 J. Yang, Z. Ma, W. Gao and M. Wei, *Chem.–Eur. J.*, 2017, **23**, 631–636.

32 X. Jiang, J. Zhang, L. Yu, R. Chen and X. Xu, *Micro Nano Lett.*, 2016, **11**, 137–141.
33 J. Yuan, B.-Y. Wang, Y.-C. Zong and F.-Q. Zhang, *Inorg. Chem. Commun.*, 2023, 110799.
34 J. Rodríguez-Carvajal, *Full Prof*, 2000, pp. 1–139.
35 M. Kaur, S. Gautam, K. H. Chae, W. Klysubun and N. Goyal, *Sci. Rep.*, 2023, **13**, 10769.
36 B.-Y. Wang, E.-D. Li, Y.-C. Zong, X.-B. Wang, J. Yuan and F.-Q. Zhang, *J. Mater. Res.*, 2022, **37**, 1070–1082.
37 G. Williamson and W. Hall, *Acta Metall.*, 1953, **1**, 22–31.
38 T. Runcevski and C. M. Brown, *Cryst. Growth Des.*, 2021, **21**, 4821–4822.
39 D. Bhatnagar, S. Gautam, H. Batra and N. Goyal, *J. Mech. Behav. Biomed. Mater.*, 2023, **142**, 105814.
40 J. Hao, Y. Jiang, X. Gao, F. Xie, Z. Shao and B. Yi, *J. Membr. Sci.*, 2017, **522**, 23–30.
41 Z. Durmus, R. Köferstein, T. Lindenberg, F. Lehmann, D. Hinderberger and A. W. Maijenburg, *Ceram. Int.*, 2023, **49**, 24428–24441.
42 R. Ramachandran, W. Xuan, C. Zhao, X. Leng, D. Sun, D. Luo and F. Wang, *RSC Adv.*, 2018, **8**, 3462–3469.
43 A. Lin, A. A. Ibrahim, P. Arab, H. M. El-Kaderi and M. S. El-Shall, *ACS Appl. Mater. Interfaces*, 2017, **9**, 17961–17968.
44 Q. He, W. Wang, N. Yang, W. Chen, X. Yang, X. Fang and Y. Zhang, *Molecules*, 2023, **28**, 6806.
45 S. Fatemi, M. R. Ganjali, et al., *J. Energy Storage*, 2022, **55**, 105545.
46 H. Huang and M. Niederberger, *Nanoscale*, 2019, **11**, 19225–19240.
47 S. Maiti, A. Pramanik and S. Mahanty, *Chem. Commun.*, 2014, **50**, 11717–11720.
48 O. Gonzlez-Meza, E. Larios-Durn, A. Gutiérrez-Becerra, N. Casillas, J. Escalante and M. Bárcena-Soto, *J. Solid State Electrochem.*, 2019, **23**, 3123–3133.
49 R. Wang, P. Wang, X. Yan, J. Lang, C. Peng and Q. Xue, *ACS Appl. Mater. Interfaces*, 2012, **4**, 5800–5806.
50 R. Kötz and M. Carlen, *Electrochim. Acta*, 2000, **45**, 2483–2498.
51 R. Ramachandran, M. Saranya, P. Kollu, B. P. Raghupathy, S. K. Jeong and A. N. Grace, *Electrochim. Acta*, 2015, **178**, 647–657.
52 A. Liu, H. Che, Y. Mao, Y. Wang, J. Mu, C. Wu, Y. Bai, X. Zhang and G. Wang, *Ceram. Int.*, 2016, **42**, 11435–11441.
53 N. S. Arul, D. Mangalaraj, R. Ramachandran, A. N. Grace and J. I. Han, *J. Mater. Chem. A*, 2015, **3**, 15248–15258.